Full Length Article

Anisotropic magneli phase Ti-suboxides in β- cyclodextrin template - Enhanced charge separation upon gold doping

Monojit Sarkar [b], Piyali Bhattacharya [a], Hirak Chatterjee [c], Sudeshna Sarkar [a], Barun Mandal [a], Sudipta Biswas [e], Sujit Kumar Ghosh [d], Swati De [a,*]

[a] *Department of Chemistry, University of Kalyani, Kalyani, Nadia-741235, West Bengal, India*
[b] *Department of Chemistry, Basirhat College (Affiliated to West Bengal State University), Basirhat, North 24 Parganas-743412, West Bengal, India*
[c] *Nanoparticle Trapping Laboratory, Department of Applied Physics, Universidad de Granada, Granada 18071, Spain*
[d] *Department of Chemistry, Jadavpur University, Kolkata 700 032, India*
[e] *Boyra Sammilani High School (H.S), Boyra, Bagdah, North 24 Parganas-743232, West Bengal, India*

A R T I C L E   I N F O

A B S T R A C T

Substoichiometric titanium oxides i.e. Magneli phase (MP) TiO_x are attractive due to their conductive nature. However, their synthesis is challenging. In this work, Anisotropic MP- Ti_4O_7 nanoparticles and Au doped nanocomposites were synthesized using β- cyclodextrin as template. The MP nanomaterials were 20-30 nm in size. The synthesis conditions were mild. These MP- TiO_x nanomaterials show efficient charge separation upon light excitation i.e. they (i) act as efficient photocatalysts; (ii) they can be sensitized by a fluorescent dye; (iii) finite element method (FEM) simulations indicate substantial interfacial plasmonic charge generation at the metal-semiconductor interface in the doped nanocomposites.

1. Introduction

The electrical conductivity of pure stoichiometric TiO_2 is quite low. It can be increased by heating in reducing environment. Such heat treatment results in sub-stoichiometric titanium oxides or magneli phase TiO_2[1]. Ti_nO_{2n-1} is the general formula of magneli phase oxides (n ranges from 3 to 10) [2]. A *semiconductor-to-metal* transition was also reported for these oxides [3]. Magneli phase (MP) Ti_nO_{2n-1}, finds application in fuel cells, lead acid batteries and also in waste water treatment [1–5]. Magnéli phase TiO_x can withstand highly oxidizing atmospheres. Among MP suboxides, Ti_4O_7 formed from three TiO_2 octahedra and one TiO octahedron has high conductivity [6].

There have been efforts to prepare MP Ti_4O_7, by the reduction of rutile phase TiO_2 at extremely high temperatures [7–11]. The high temperature promotes sintering. However, in such synthesis, the diameter of the particles was large (0.5 nm to 1μm). Efforts were made by Ioroi et.al [12] and Portehault et al. [13] to synthesize smaller titania clusters with large surface area. Ti_4O_7 is usually synthesized via two routes: (i) Carbothermal treatment and (ii) calcination in hydrogen atmosphere [2,12,14-18].

$$nTiO_2 + ½ C \; Ti_nO_{2n-1} + ½ CO_2 \; [] \tag{1}$$

Wu et. al used glucose as the carbon source in the carbothermal method [4].

More recently, colloidal self-assembly has been used in presence of organic templates to for preparing nanoparticles [19–22]. Such self-assembly of nanoparticles imparts control over particle size, particle shape and surface area. Cyclodextrins (CDs) are water soluble cyclic sugars which possess a hydrophobic internal cavity and a hydrophilic surface [Scheme S1, Supporting Information] [23–25]. Among cyclo-dextrins, β- Cyclodextrin is more cost effective, and has been widely used in the past as templates for preparing nanoparticles [26–29]. CD aggregates have sizes in the range 200-300 nm [30–32]. Additionally, the primary OH group aids in reduction of metal ions [33]. Higher CD concentration leads to smaller particles [34].

Apart from synthesis of MP- titanium oxide, another aim of the present work was to explore metal doped titanium oxide materials. It is known that doping of noble metal nanoparticles (Au, Ag, Pd) in semiconductor materials can increase the photocatalytic activity of the latter [35–38]. Herein, we report the successful synthesis of MP- Ti_4O_7 nanoparticles and Au doped MP- Ti_4O_7 nanocomposites by a sono-chemical method using β-CD as a template and citrate as reductant. The added advantage is that the synthesis was carried out at ambient

temperature. Citrate acts both as a stabilizer and as a reducing agent for formation of Au NPS *in-situ* from HAuCl$_4$. β-CD helps in controlling the size of the particles. Interesting anisotropic structures comprising the Magneli Phase nanomaterials were obtained. These MP nanomaterials were found to function as very efficient photocatalysts for the degradation of the pollutant dye Malachite green (MG). The MP nanomaterials were also found to be effectively sensitized by a fluorescent dye thus indicating their suitability for use in dye sensitized solar cells. Additionally finite element method (FEM) simulations were performed, the results of which lend support to the Photocatalysis and fluorescence results.

2. Experimental section

2.1. Materials

Titanium (IV) isopropoxide was obtained from Sigma-Aldrich and used without further purification. Tetrachloroauric acid (HAuCl$_4$.3H$_2$O), Isopropanol, Nitric Acid (HNO$_3$) were obtained from Aldrich (Merck India). β-cyclodextrin was obtained from Spectrochem Pvt. Ltd. Trisodium citrate dihydrate was obtained from Merck Life Science Pvt. Ltd. Malachite Green was obtained from Qualigens Fine Chemicals. Fluorescein dye, used for the fluorescence studies, was obtained from Fluka. All the experiments were performed in double distilled water.

2.2. Methods

2.2.1. Synthesis of MP-TiO$_x$ nanomaterials using β-cyclodextrin
1:1 isopropanol and water mixture was taken and its pH adjusted (pH 3-4) using concentrated HNO$_3$. 1 × 10^{-3}M β-cyclodextrin (β-CD) was then added and the mixture stirred vigorously. Subsequently, Titanium precursor (Ti-isopropoxide) dissolved in isopropanol was added drop wise to the mixture (final concentration 2 × 10^{-3}M). After slight stirring trisodium citrate solution (2 × 10^{-3}M) was added. The whole mixture was then sonicated at 50–60°C. The resultant mixture was stirred at 120–150°C overnight. This resulted in production of colloidal MP-TiO$_2$ nanoparticles via hydrolysis of the precursor accompanied by condensation.

2.2.2. Synthesis of Au- doped MP-TiO$_x$ nanocomposites
1:1 isopropanol and water mixture was taken and its pH adjusted (pH 3-4) using concentrated HNO$_3$. 1 × 10^{-3}M β-cyclodextrin (β-CD) was then added and the mixture stirred vigorously. Subsequently, Titanium precursor (Ti-isopropoxide) dissolved in isopropanol was added drop wise to the mixture (final concentration 2 × 10^{-3}M). After slight stirring trisodium citrate solution (2 × 10^{-3}M) was added. Gold precursor (HAuCl$_4$) solution was then added, keeping final concentration 2 × 10^{-4} M. The whole mixture was then sonicated at 50-60°C and then stirred at 120-150°C and made to stand overnight. Pink coloured colloidal solution of Au MP- Ti$_4$O$_7$ nanocomposites was thus prepared.

2.3. Instrumentation

The absorption spectra of the nanoparticles/nanocomposites were recorded with a Shimadzu spectrophotometer, Model No. UV2401PC. Powder X-ray diffraction (XRD) data were recorded using a Bruker D8 advanced powder X-ray diffractometer employing CuKα radiation (λ = 1.5418Å). TEM studies of the nanoparticles were carried out at a resolution of 1.9 Å with a JEOL, JEM-2100 electron microscope from Japan. Scanning Electron Microscope (SEM) studies were carried out with a EVO-LS10, CARL- ZEISS instrument, UK. The optical constants of the nanomaterials were determined using a J. A. Woolam M-2000 spectroscopic ellipsometer. A Horiba Fluoromax 4 Spectrofluorimeter was used for the steady-state fluorescence studies.

The fluorescence lifetimes were measured with a setup from Horiba

Jobin Yvon employing time-correlated single-photon counting (TCSPC) technique. A 405 nm laser was used as the excitation source. The photocatalytic studies were carried out using a Philips UV-lamp (15 W). Numerical simulation based on finite element method (FEM) was performed using COMSOL Multiphysics software package. The optical constants of bulk gold and TiO$_2$ determined from ellipsometry were used in the calculations.

3. Results and discussion

3.1. Characterization of the nanomaterials

3.1.1. UV-visible absorption spectra
The absorption spectrum of the synthesized MP-Ti$_4$O$_7$ nanocomposites is illustrated in [Fig. 1(a)]. The band gap (Eg) of the synthesized titania nanoparticles was determined using the Kubelka–Munk plot [Fig. 1(c,d)]. The absorption edge of synthesized MP- Ti$_4$O$_7$ was at 362 nm, corresponding to a band gap of 3.74 eV [Fig. 1(c)]. The formation of Au-Ti$_4$O$_7$ nanocomposites was noted from the purple coloration of the solution and the absorption spectra [Fig. 1(b)]. The absorption edge of the Au-Ti$_4$O$_7$ nanocomposites was at 366 nm, corresponding to a band gap of 3.67 eV [Fig. 1(d)]. E$_g$ decreases in the nanocomposites as the deposition of Au on Ti$_4$O$_7$ nanoparticles causes transfer of photoexcited electrons to the Fermi level of the noble metal leading to faster electron hole pair separation in the nanocomposite [Scheme 1].

The molar ratio of β-CD/ Ti precursor in the synthesis of both MP-Ti$_4$O$_7$ and Au-doped Ti$_4$O$_7$ was maintained at 0.2 and β-CD/Au precursor molar ratio for the latter was 5. A mixture of different morphologies was achieved comprising icosahedra, triangular nanoplates, nanorods and cubes. Bleta et al [39] prepared titania nanoparticles in aqueous phase via a colloidal self-assembly approach using various cyclodextrins (CDs) as structure directing agents. They had reported that β-CD/ TiO$_2$ molar ratio of 0.076 produced a mixture of anatase, rutile and brookite phases of TiO$_2$. The percentages of different phases were found to vary with β-CD/ TiO$_2$ ratio. Kochkar et.al reported the synthesis of shape-controlled Ag nanoparticles using β-CD as a shape-controlling agent [40]. At different molar ratios of β-CD/ Ag such as 50, 80 and 150, a mixture of inter-twinned icosahedrons, nanorods, triangular nanoplates and bipyramids were produced. It was noticed that the percentage of icosahedral NPs increased upon increasing the molar ratio of β-CD/ Ag.

3.1.2. X-ray diffraction
The powder X-ray diffraction patterns of both the synthesized samples are shown in Fig. 2. From Fig. 2(a), the formation of several MP-titanium sub-oxides was noted. The sharp peaks at 2θ equal to 29.31°, 31.90° and 35.37° correspond respectively to the [122], [022] and [114] planes of sub-stoichiometric Ti$_4$O$_7$ [JCPDS No. 181402]. 2θ values of 42.46°, 47.93° and 56.5° correspond respectively to the [004], [312] and [020] planes of β-Ti$_3$O$_5$ [JCPDS No. 230606] while 2θ values of 18.9° and 55.65° correspond respectively to the [202] and [406] planes of γ-Ti$_3$O$_5$ [JCPDS No. 270905].

Fig. 2(b) shows the same peaks of Ti$_4$O$_7$ and other sub-oxides along with additional peaks of Au, 2θ equal to 38.23°, 44.4°, 64.79° and 77.72° corresponding respectively to the [111], [200], [220] and [311] planes, [JCPDS No. 040784]. This indicates the formation of Au -Ti$_4$O$_7$ nanocomposites.

The average crystallite size D was calculated from the Scherrer formula,

$$D = \frac{k\lambda}{\beta \cos\theta} \tag{2}$$

K= the shape factor (a value of 0.9 was used in this study)
λ = X-ray wavelength (1.54056 Å for Cu Kα)
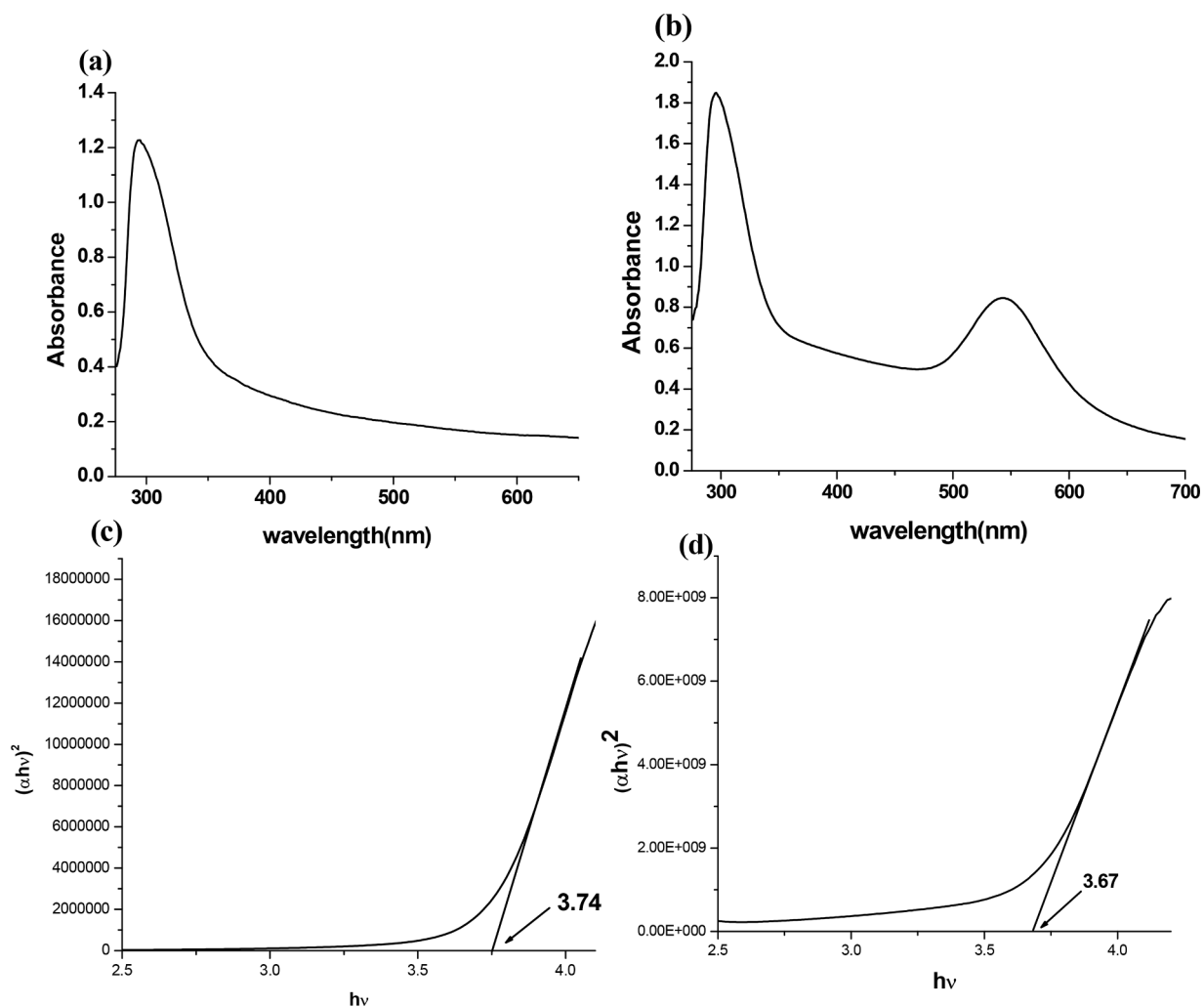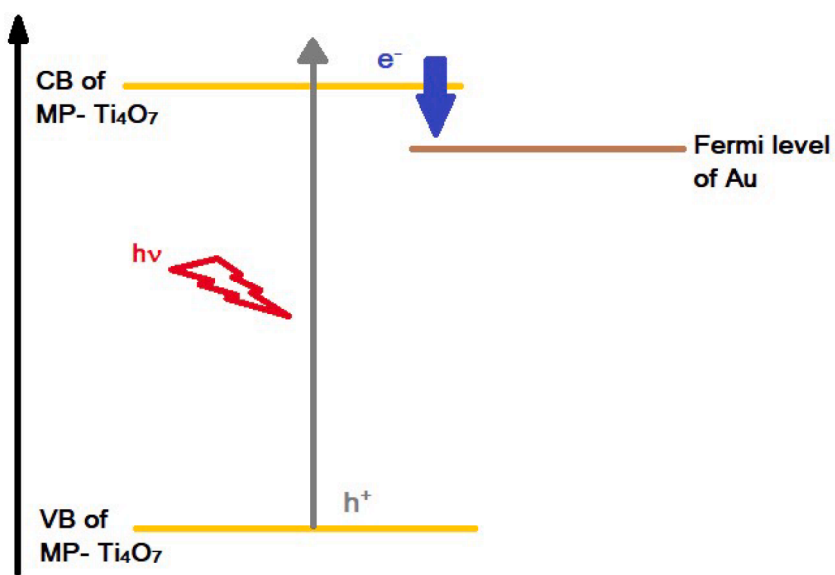β = Full width at half-maximum (FWHM), after subtracting the

Fig. 1. UV-Vis Absorption spectrum of (a) MP-Ti_4O_7 nanoparticles and (b) Au-MP-Ti_4O_7 nanocomposites. Bandgap plots for (c) MP-Ti_4O_7-nanoparticles and (d) Au-MP-Ti_4O_7 nanocomposites.

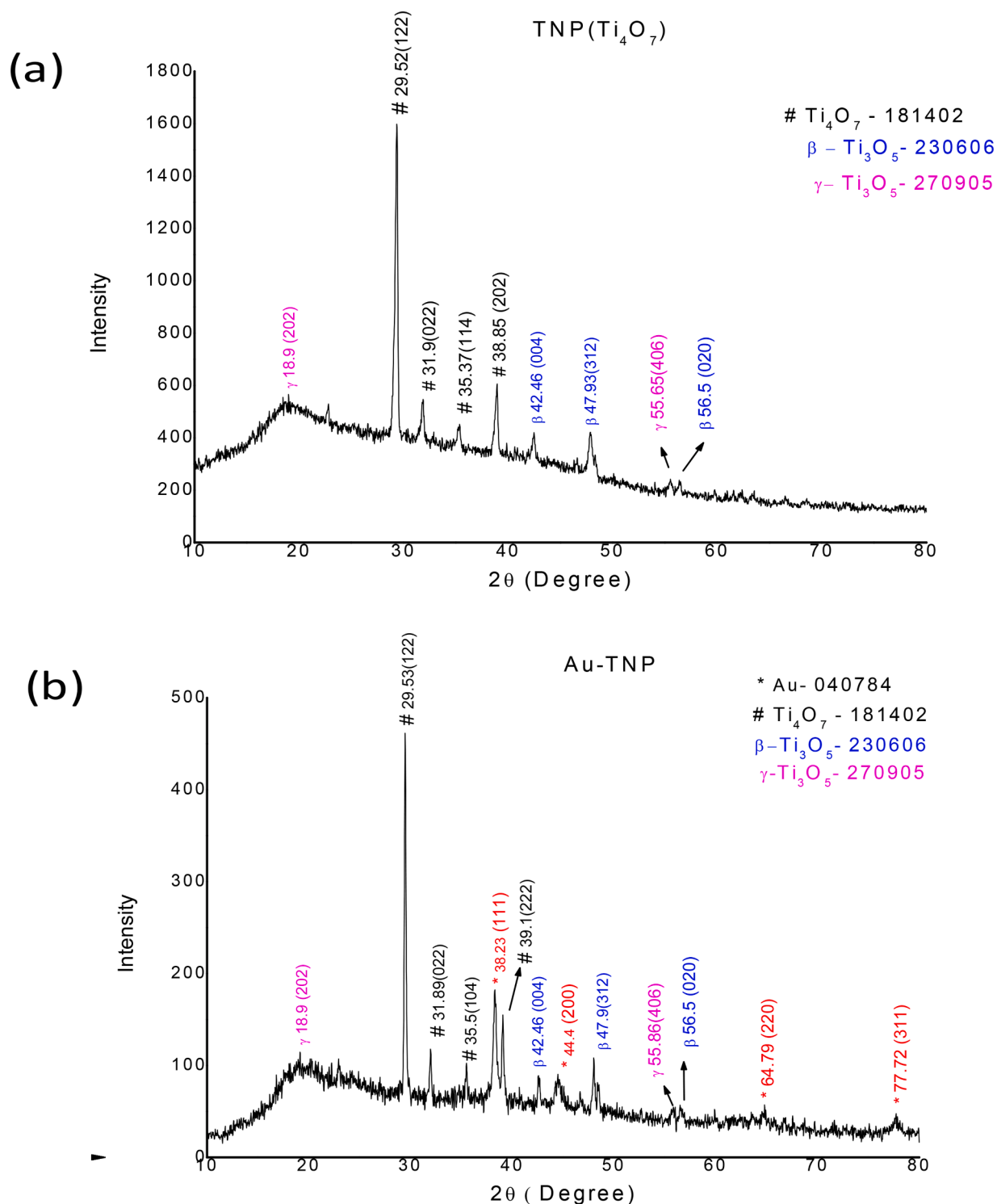**Scheme 1.** Efficient electron-hole separation in Au-MP-Ti_4O_7 nanocomposites.

(a)

TNP(Ti$_4$O$_7$)

Ti$_4$O$_7$ - 181402
β – Ti$_3$O$_5$ - 230606
γ– Ti$_3$O$_5$ - 270905

29.52(122)

γ 18.9 (202)

31.9(022)

35.37(114)

38.85 (202)

β 42.46 (004)

β 47.93(312)

γ 55.65(406)

β 56.5 (020)

Intensity

2θ (Degree)

(b)

Au-TNP

* Au- 040784
# Ti$_4$O$_7$ - 181402
β−Ti$_3$O$_5$- 230606
γ-Ti$_3$O$_5$- 270905

29.53(122)

γ 18.9 (202)

31.89(022)

35.5(104)

* 38.23 (111)

39.1(222)

β 42.46 (004)

* 44.4 (200)

β 47.9(312)

γ 55.86(406)

β 56.5 (020)

* 64.79 (220)

* 77.72 (311)

Intensity

2θ (Degree)

Fig. 2. Powder XRD pattern of (a) MP-Ti$_4$O$_7$ nanoparticles and (b) Au-doped MP-Ti$_4$O$_7$ nanocomposites.

instrumental line broadening.

θ = Bragg angle

The calculated crystallite size of MP-Ti$_4$O$_7$ is about 25 nm and 35 nm in case of Au-doped MP-Ti$_4$O$_7$.

3.1.3. Electron Microscopy results

The synthesized MP-Ti$_4$O$_7$ and Au doped MP-Ti$_4$O$_7$ nanomaterials were characterized by scanning electron microscopy (SEM) and transmission electron microscopy (TEM). The SEM images are shown in Fig. 3. Fig. 3(a) and 3(b) show that a homogeneous distribution of

cuboidal materials is formed in high yield. These materials have dimension > 100 nm. Thus, these may actually indicate β-CD cages (comprising few β-CD) molecules) encapsulating the MP-Ti-suboxide nanoparticles. For the Au-Ti suboxide nano composites too, the cuboid dimensions are the same, only number density decreases. Thus in all probability, these cuboids are truly CD cages or aggregates. These encapsulate the nanomaterials. In Fig. 3(c), the SEM result for Au doped MP-Ti$_4$O$_7$ indicates that for the composites icosahedral/ triangular entities are formed.

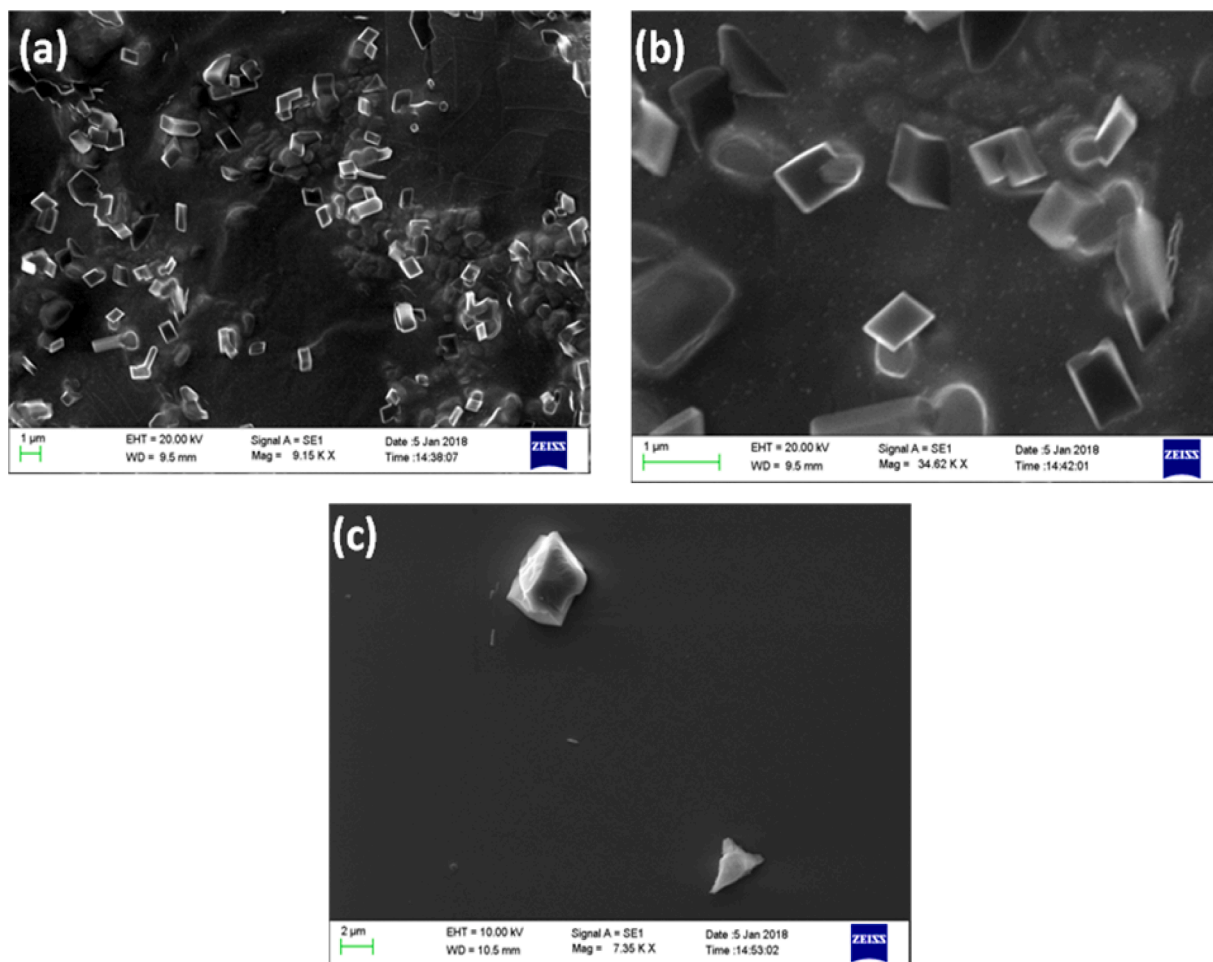The TEM images of MP-Ti sub oxides are shown in Fig. 4(a and b) and

Fig. 3. (a,b). SEM images of MP-Ti$_4$O$_7$ nanomaterials and (c) Au-doped MP-Ti$_4$O$_7$ nanocomposites.

they indicate that icosahedral structures are formed. Selected area electron diffraction (SAED) pattern Fig. 4(d) shows bright spots with definite rings, which indicates the crystalline nature of the synthesized nanoparticles. Fig. 4(c) shows the HRTEM image of the nanoparticles. Well-resolved lattice fringes can be observed in the HRTEM image, the d-spacing of 0.311nm corresponds to the (022) plane of the Ti$_4$O$_7$ and 0.302 nm corresponds to the (122) plane of Ti$_4$O$_7$ nanoparticles. Thus the nanoparticles observed in TEM represent the MP-Ti$_4$O$_7$ sub oxide predominantly. The particle dimension is ∼ 20 nm.

On the other hand, the TEM images of Au-doped Ti$_4$O$_7$ are shown in Fig. 5. Various types of icosahedral and triangular nanocomposites are seen in [Fig. 5(a)]. SAED pattern [Fig. 5(c)] shows distinct diffraction rings with spots, which indicates that the particles are poly crystalline. Fig. 5(b) shows the HRTEM image. From the d-spacing, 0.235 nm corresponds to (111) plane of Au and 0.29 nm corresponds to (122) plane of Ti$_4$O$_7$, confirming the formation of Au doped Ti$_4$O$_7$. The equilateral triangle shaped nanocomposite has an edge length of ∼30 nm thus the nanocomposites are larger than the Ti$_4$O$_7$ NPs. HRTEM shows lattice planes corresponding to both Au and Ti$_4$O$_7$ confirming the composite nature. This is also confirmed by EDX Fig. 5(d).

The SEM images of the MP-Ti$_4$O$_7$ and Au-doped MP-Ti$_4$O$_7$ nano materials [Fig. 3(a,b and c)] were found to have bigger dimensions than that seen in the TEM images [Fig. 4(a and b) and Fig. 5(a and b)]. From HRTEM image (Fig. 5b) it is evident that fringes of both Au and Ti$_4$O$_7$ coexist. So it can be said that Au and Ti$_4$O$_7$ grow simultaneously side by side in the same lattice. β- CD acts as template for synthesizing the nanostructures.

Energy dispersive X-ray spectroscopy (EDX) was employed to

ascertain the composition of the synthesized nanoparticles. The EDX analysis [Fig. 5(d)] indicates the presence of Au, Ti and O proving that the *as-synthesized* nanomaterials are composed of Au-doped Ti$_4$O$_7$.

Summarizing, the electron microscopy results indicate that anisotropic MP-Ti$_4$O$_7$ and Au-doped MP-Ti$_4$O$_7$ nanomaterials are formed within the β–CD cages. The distinct advantage of using β–CD being that the confined dimension within the β–CD cavity arrests the growth of the nanomaterials restricting the size to ∼10-15 nm edge length.

Another plausible reason for the small size of the nanomaterials could be the use of the sonochemical method of synthesis. When ultrasonic waves pass through the reaction mixture containing β-CD, sodium citrate and Ti-precursor, a large number of micro bubbles are formed, these subsequently grow and then collapse in a very short time, about a few microseconds. This is referred to as ultrasonic cavitation. This results in ultrasonic cavitation which can generate local temperature as high as 5000 K and local pressure as high as 500 atm [41]. The temperature and pressure generated from the collapse of water bubbles is high enough to dissociate water molecules into primary hydrogen radicals (H•) and hydroxyl radicals (OH•) during cavitation [42,43]. The standard reduction potential of H• is, E^0 (H$^+$/ H•) = - 2.3 V *vs*. NHE and OH•, E^0 (H$_2$O/ OH•) = 2.7 V *vs*. NHE (NHE= Normal Hydrogen Electrode) in acidic solution. Therefore, H• can act as a very strong reducing agent, while OH• has a strong oxidizing ability. These active species can drive the chemical reactions and lead to predominance of the rate of formation of MP-Ti$_4$O$_7$ and Au nuclei over the slower rate of particle growth. Thus nanoparticles / nanocomposites of controlled size are formed. The strongly reducing radicals formed during ultrasonic cavitation lead to a large number of nuclei that probably form
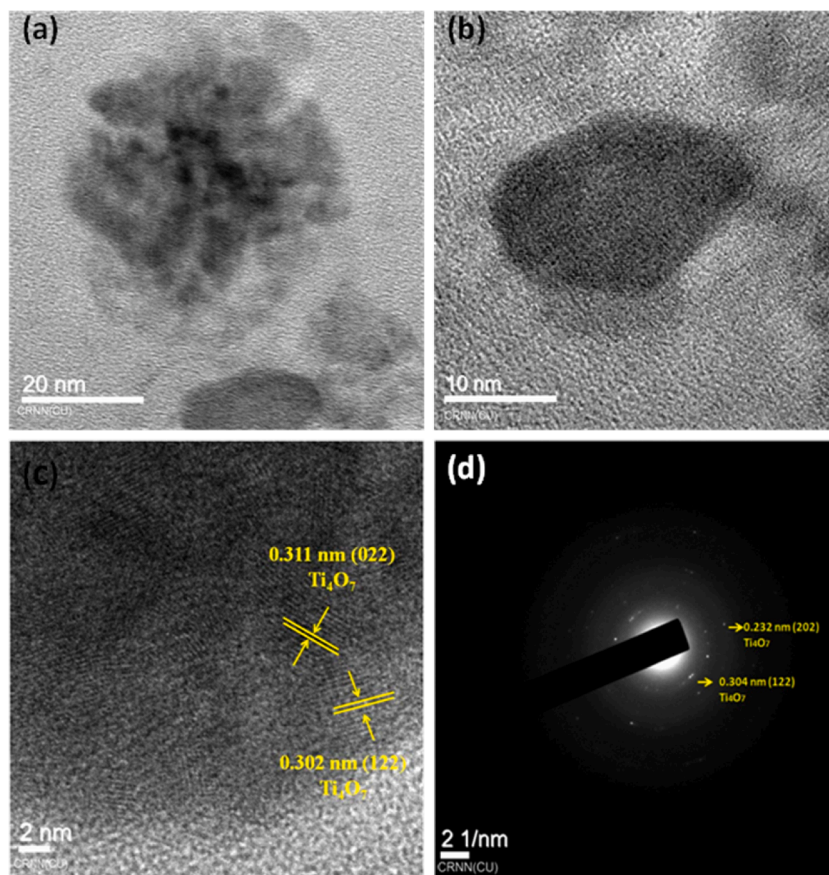
Fig. 4. (a,b) TEM images, (c) HRTEM image and (d) SAED pattern of MP-Ti$_4$O$_7$ nanomaterials.

instantaneously and subsequent growth is arrested within the β–CD cavity.

3.2. Photocatalytic activity of the nanoparticles

Malachite green (MG), a cationic dye is widely used as a fabric dye. MG is highly toxic and has been implicated in carcinogenesis and respiratory toxicity [44]. Therefore, the removal of MG from industrial wastewater is very important. Additionally MG has been widely used as fungicide in the fish industry. Although it has been banned in certain countries, its illegal use is still rampant in many parts of the globe. Considering the extremely hazardous nature of the dye it is important to devise methods for its degradation and removal. Semiconductors can cause degradation of organic contaminats via photo induced generation of charge carriers [45]. TiO$_2$ based materials have been used as photocatalysts in the past due to their suitable band gap energy, chemical stability, non-toxicity and high photocatalytic activity [46–48].

When a photon with suitable energy is incident on the semiconductor, an electron (e$^-$) is promoted from the valence band (VB) into the conduction band (CB) leaving a hole (h$^+$). Now, the electron in the CB and hole in the VB have several pathways. They can (i) recombine; (ii) get trapped in localized surface states; (iii) react with electron donors and acceptor molecules adsorbed on the semiconductor surface. In the absence of suitable electron and hole scavengers, the excited state energy is lost by fast recombination [49]. If a suitable scavenger or surface defect state is available to trap the charge carriers, recombination is prevented and subsequent redox reactions may occur. The holes in the valence band are strong oxidants (+1.0 to +3.5 V *vs.* NHE), while the electrons in the conduction-band are good reductants (+0.5 to -1.5 V *vs.* NHE) [50].

Magneli phases of Ti$_n$O$_{2n-1}$ were earlier shown to be efficient photocatalysts [51]. The "n" values in the stoichiometric formulae were shown to be important factors affecting the photoactivity, smaller the n-values (e.g for Ti$_2$O$_3$ and Ti$_3$O$_5$) more was the photoactivity. This effect was assigned to the larger number of oxygen vacancies in lower "n" value MP oxides e.g. 1/4 of oxygen lattice sites are vacant in Ti$_2$O$_3$ [51].

It seemed natural to thus explore the photocatalytic activity of the titania materials synthesized in this work. The reaction chosen was the light induced degradation of the dye pollutant MG. MG dye has a strong absorption at 617 nm as shown in Fig. 6(a) [52]. For photocatalysis, dye adsorption on the photocatalyst surface in the dark is important. The E_g value of MP-Ti$_4$O$_7$ obtained earlier (Fig. 1c) corresponds to 332 nm wavelength, thus UV light was used for the photocatalysis study. MG degradation was performed using initial dye concentration of 1×10^{-5} M. 500 μl of colloidal photocatalyst suspension was added to 10 ml dye solution. The degradation study was also performed in absence of any photocatalyst. In absence of photocatalyst, MG shows nominal photodegradation upon UV irradiation [Fig. 6(a)]. But in presence of the MP-titania photocatalysts, significant photocatalytic effects were observed [Fig. 6(b and c)]. The Au-doped MP-Ti$_4$O$_7$ nanocomposites were superior photocatalyst in comparison to undoped MP- Ti$_4$O$_7$ [inset of Fig. 6(c)]. After one hour, 98% of dye was degraded by the Au-doped MP-Ti$_4$O$_7$ nanocomposites while 90% was degraded by the MP-Ti$_4$O$_7$ nanoparticles. Scheme 2 depicts the mechanistic pathways of MG degradation by both MP-Ti$_4$O$_7$ and Au-doped MP-Ti$_4$O$_7$ nanocomposites.

Photocatalytic rate constants were 11.8×10^{-2} min^{-1} for Au-doped MP-Ti$_4$O$_7$ nanocomposites and 8.29×10^{-2} min^{-1} for undoped MP-Ti$_4$O$_7$. The narrower band gap of Au-doped Ti$_4$O$_7$ compared to Ti$_4$O$_7$ nanoparticles and the proximity of the Fermi level of Au to the conduction band of MP-Ti$_4$O$_7$ [Scheme 1], leads to enhanced electron-hole separation in the nanocomposites thus improving their photocatalytic
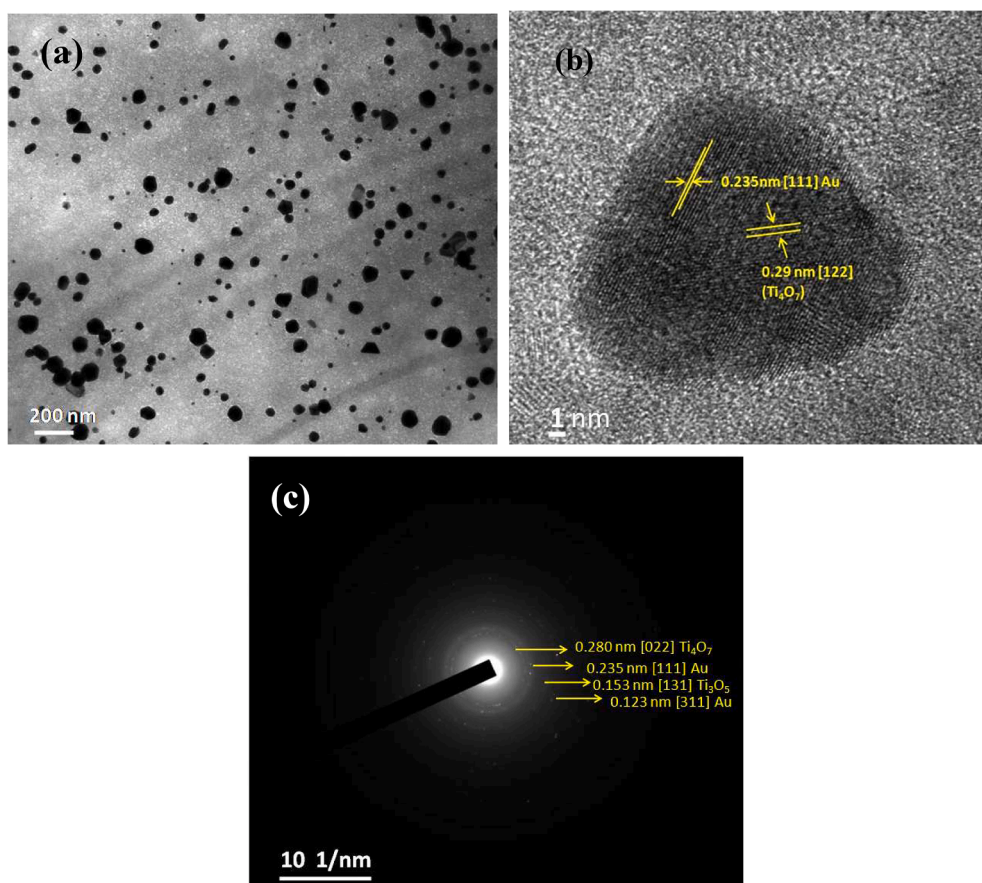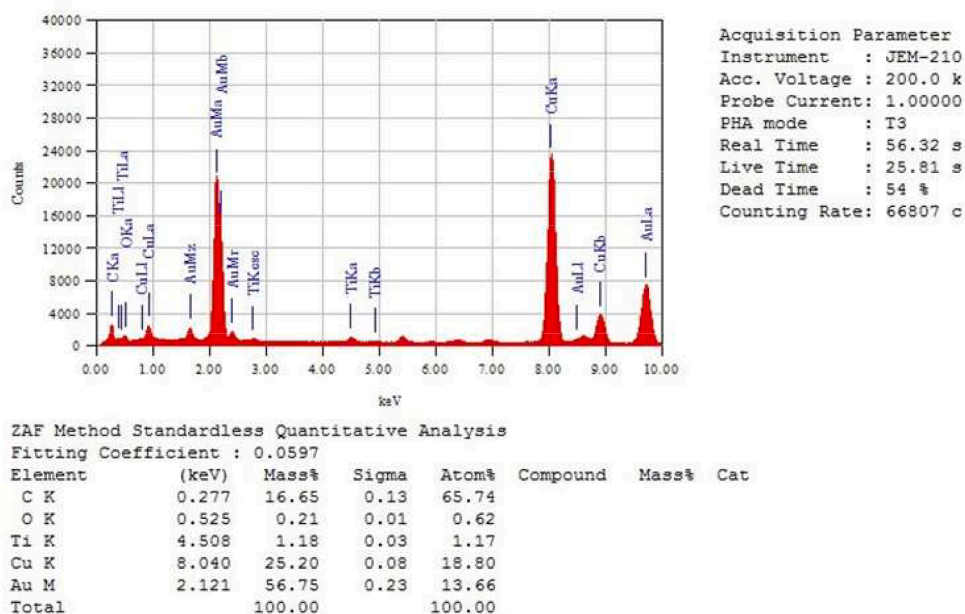
Fig. 5. (a) TEM image, (b) HRTEM image, (c) SAED pattern and (d) EDX of Au-doped MP-Ti_4O_7 nanocomposites.

performance [53,54]. Upon UV exposure of the nanocomposite, the electron transfer from the excited MP-Ti_4O_7 to Au becomes facile as the Fermi level of Au is lower than the conduction band of MP-Ti_4O_7. This increases the reducing ability of the composite [55]. Thus the increased charge separation and increased reducing power cause enhanced

photocatalytic activity.

Additionally it is known that for anisotropic particles catalytic activity is high at the edges and corners [56–58]. Both the nanocomposites and the undoped MP-Ti_4O_7 nanoparticles are anisotropic. In the past too, anisotropic metal nanostructures exhibited superior optical and
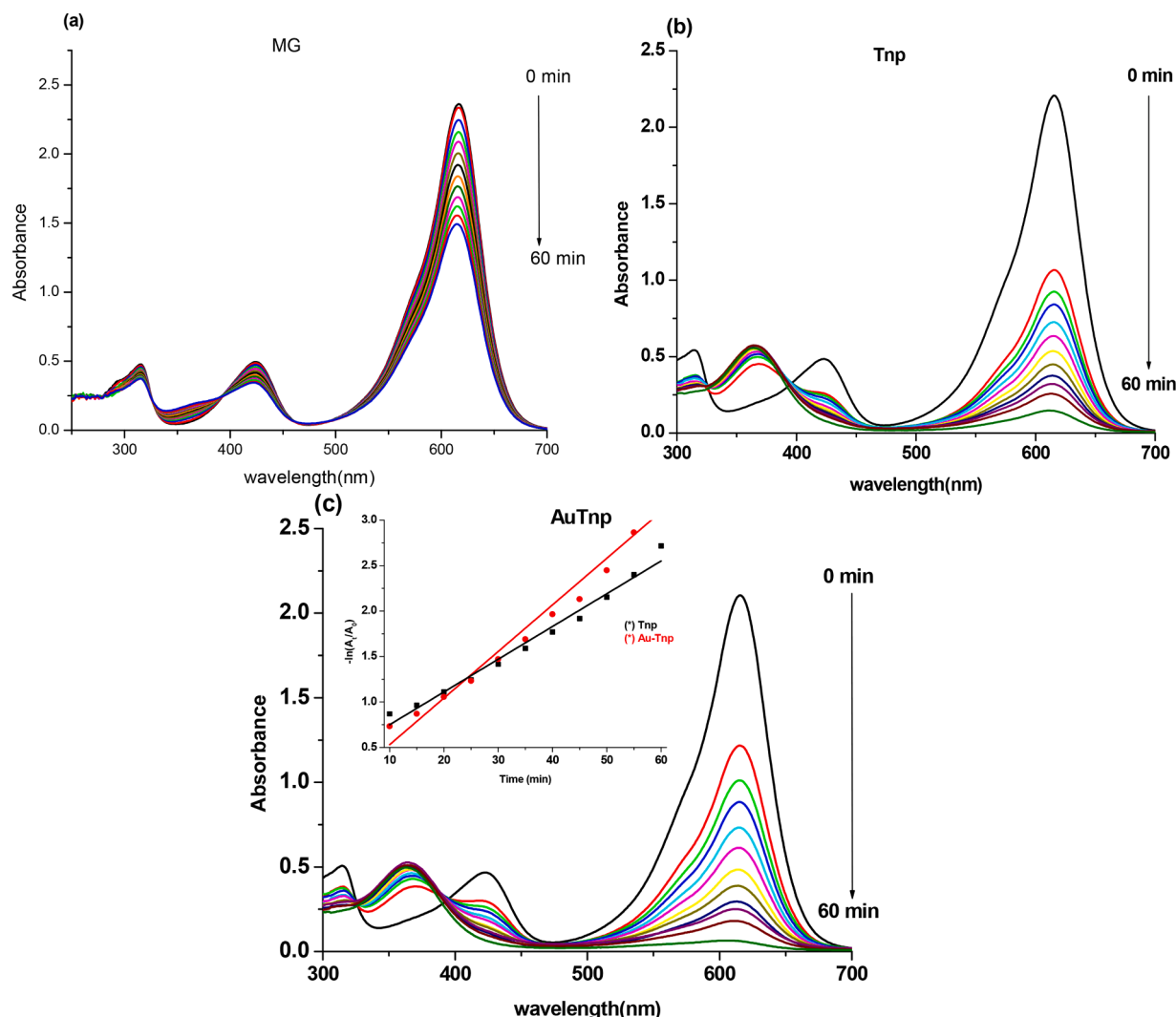
Fig. 6. Photocatalytic degradation of Malachite Green upon UV irradiation (a) without any catalyst (b) with MP-Ti$_4$O$_7$ nanoparticles (c) with Au-doped MP-Ti$_4$O$_7$ nanocomposites, (inset) efficiency curve for MG degradation using MP-Ti$_4$O$_7$ and Au doped MP-Ti$_4$O$_7$.

charge transport [59]. Thus anisotropy in the structures of the nanomaterials synthesized in this work could lead to better photocatalytic activity. To verify this assumption, FEM simulation studies were performed.

The FEM simulation of the triangular Au-doped MP-Ti$_4$O$_7$ nanocomposites [Fig. 5(b)] shows enhanced charge generation which is clear from the electromagnetic field at the interface. For the simulation, the refractive indices were determined directly from ellipsometric data shown in Fig. 7(a), Johnson –Christy database [60] and Aspnes' database [61] was employed to for simulation of the optical response from gold and silicon, respectively. The FEM simulation results on an assembly of periodically stacked triangular gold (top) particle, MP-Ti$_4$O$_7$ (intermediate) and Si (base) is shown in Fig. 7(b) given below. The angular dependence of the polarized incident beam, for both plasmonic (543 nm) and non-plasmonic (296 nm) excitation on the charge transfer at the interface is shown. It is seen that for an increase in the azimuthal angle by 5°, the plasmon *on and off* conditions for surface charge generation occur alternatively. For angles of 40°, 50° and 60° the resultant wave gets fully reflected by the edge of the top gold nanoprism which is present on the composite [Fig. 7(b)]. In contrast, for other angles, the orientation on the plane makes the plasmonic field excited.

Thus the FEM simulations indicate that plasmonic charge generation at the metal-semiconductor interface helps the band electrons to overcome and cross the band gap. This agrees with the situation shown in

Scheme 1 and also explains the enhanced photocatalytic efficiency of the Au-doped MP-Ti$_4$O$_7$ nanocomposites. For such dielectric surfaces in close contact, collective Plasmon oscillations cause increase in local electric field. This in turn leads to strong electromagnetic confinement between adjoining layers in nanocomposites. Thus the electron transfer becomes more facile for wavelengths ranging from 580 nm onwards as shown in Fig. 7. Thus from the simulated interfacial fields for both *plasmon off- and on-* conditions in the nanocomposites, evidence of greater charge accumulation is obtained. This has prospective applications of the nano composites for solar cell applications due to improved absorptivity.

Thus the photocatalysis study and the FEM analysis both indicate efficient charge separation particularly on the Au-MP-Ti$_4$O$_7$ surface/ interface. To lend more definite evidence to this conclusion, fluorescence studies were undertaken to ascertain whether electron transfer can occur from a fluorescent dye to the semiconductor and metal/ semiconductor interface.

3.3. Sensitization of MP-Ti$_4$O$_7$ nanoparticles and Au-MP-Ti$_4$O$_7$ nanocomposites by FL dye

Photosensitization studies were performed with the fluorescent dye fluorescein (FL) to assess the viability of using the FL- MP-Ti$_4$O$_7$ system for future use in dye sensitized solar cells (DSSCs). In the past, several
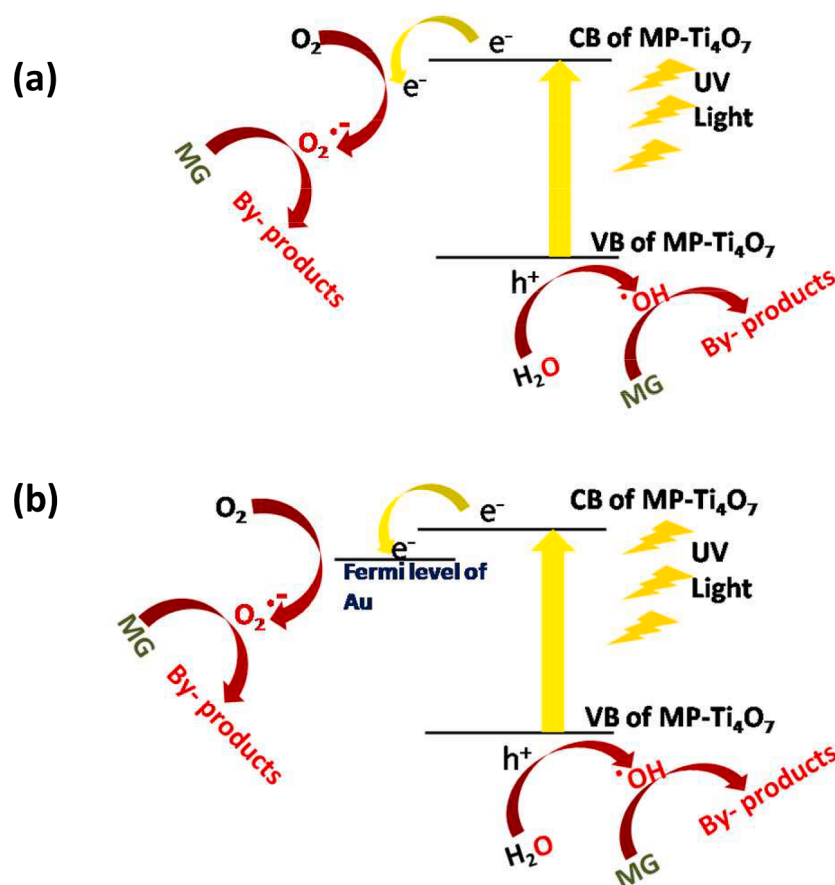
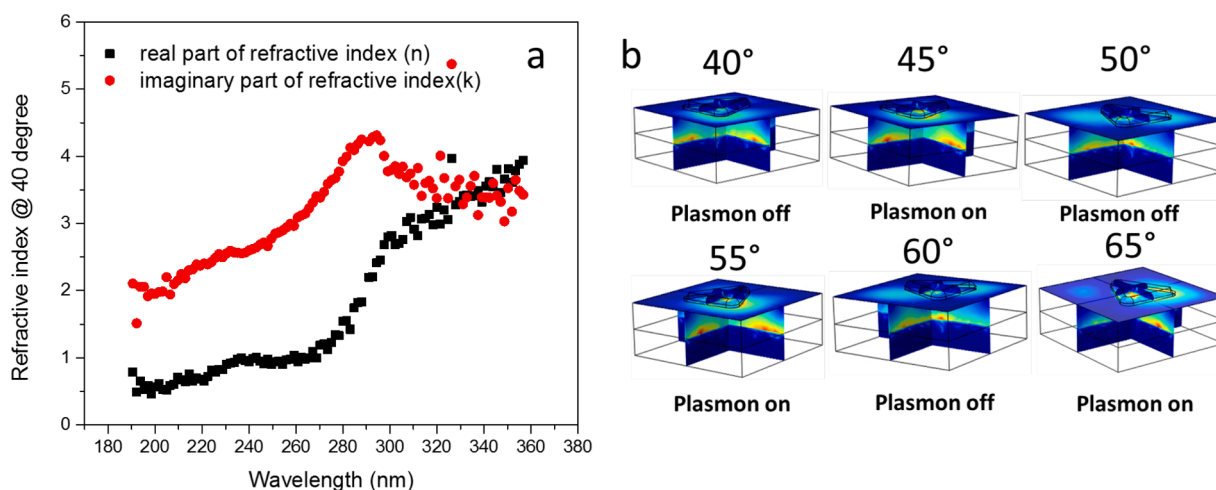**Scheme 2.** Mechanistic pathways of MG degradation by (a) MP-Ti$_4$O$_7$ and (b) Au-doped MP-Ti$_4$O$_7$ nanocomposites.

Fig. 7. (a) Representative experimental refractive indices with incident wavelength, (b) Plasmonic response of Au-doped MP-Ti$_4$O$_7$ at different angular incidence of polarized beam. Plasmon *on and off* conditions refer to calculations involving excitation in gold plasmon band regime.

research groups have reported working DSSCs using the FL- TiO$_2$ system.

3.3.1. Steady- state studies

To understand the electron transfer process in the prepared nanocomposites, fluorescence studies were performed with a highly fluorescent dye, Fluorescein (FL). Xanthene dyes like FL show interesting pH dependent equilibria in solution. Earlier studies have reported that FL can exist in four protolytic forms depending upon the pH of the medium [62–64]. Each of these four protolytic forms exhibit interesting spectral behavior. Table 1 summarizes the spectral characteristics of the four protolytic species.

Among the four species, the FL dianion has the highest quantum yield (0.93) followed by monoanion (0.37), neutral dye (0.30) and dye cation (0.18) [63].

Fluorescence emission spectra of FL were recorded in presence of increasing concentrations of MP-Ti$_4$O$_7$ nanomaterials and Au doped MP-Ti$_4$O$_7$ nanocomposites. The concentration of FL dye was maintained at 3 × 10^{-6} M to eliminate the effect of dye aggregation. The absorption

Table 1

Spectral characteristics of different protolytic forms of FL.

Protolytic forms of Fluorescein (FL)	Absorption characteristics	Fluorescence characteristics
Cation	$\lambda_{abs}{}^{max}$ = 437 nm	$\lambda_{em}{}^{max}$ = 445 nm; φ_f = 0.18
Neutral	$\lambda_{abs}{}^{max}$ =435 nm, shoulder at 475 nm	$\lambda_{em}{}^{max}$ = 515 nm; φ_f = 0.30
Monoanion	$\lambda_{abs}{}^{max}$ =475 nm, shoulder at 440 nm	$\lambda_{em}{}^{max}$ = 515 nm; φ_f = 0.37
Dianion	$\lambda_{abs}{}^{max}$ = 485 nm, shoulder at ~ 460 nm	$\lambda_{em}{}^{max}$ =515 nm; φ_f = 0.93.

spectra given below [Fig. 8(a)] indicate the presence of the monoanion of FL under the experimental conditions (peak at 475 nm and a shoulder at 455 nm). In presence of increasing aliquots of MP- Ti_4O_7 nano-materials the absorbance at 475 nm decreases and the shoulder at 455 nm becomes more prominent. This indicates conversion of the absorbing species from FL monoanion to neutral dye. The fluorescence emission spectra [Fig. 8(b)] indicate quenching of dye fluorescence in presence of increasing aliquots of MP-Ti_4O_7 nanomaterials. Now quenching of dye fluorescence can occur due to (i) dye aggregation; (ii) change of proto-lytic form or due to (iii) electron transfer from the dye excited state to the semiconductor MP-Ti_4O_7. The fluorescence excitation spectra [Fig. 8 (c)] rule out the presence of dye aggregates. Thus quenching of dye fluorescence can be either due to change of protolytic forms or electron transfer. This will be examined in details later. The Stern-Volmer plot for fluorescence quenching of FL by MP- Ti_4O_7 nanomaterials given in Fig. 8 (d) yields a Stern- Volmer constant (K_{sv}) of 5.37×10^4 M^{-1}.

In presence of increasing aliquots of Au doped MP-Ti_4O_7 nano-composites, the absorbance at 475 nm decreases and the shoulder at 455 nm becomes more prominent [Fig. 9(a)]. This indicates conversion of

the absorbing species from FL monoanion to neutral dye. The fluorescence emission spectra [Fig. 9(b)] indicate quenching of dye fluorescence in presence of increasing aliquots of Au doped MP-Ti_4O_7 nanocomposites. The fluorescence excitation spectra [Fig. 9(c)] rule out the presence of dye aggregates. Thus quenching of fluorescence can be either due to change of protolytic forms or electron transfer. This will be examined in details later. The Stern-Volmer plot for fluorescence quenching by Au- doped MP- Ti_4O_7 given in Fig. 9(d) yields a Stern-Volmer constant (K_{sv}) of 8.35×10^5 M^{-1}.

It remains to be ascertained whether the ~55% and ~65% fluorescence quenching observed in presence of MP- Ti_4O_7 nanomaterials and Au-doped MP-Ti_4O_7 nanocomposites respectively is entirely due to electron transfer from dye to nanocomposites or is partially due to change of protolytic form of dye. This was done by recording the spectra in absence of the nanocomposites while maintaining the same medium. The results are shown in **Fig. S1, Supporting Information**. It can be seen from **Fig. S1 (b).** that the fluorescence quenching due to mere change of protolytic forms of FL in solutions of different pH is much less than that seen in presence of the nanomaterials. **Fig. S1 (d).** indicates that decrease in fluorescence due to change in protolytic form of FL is only about 30%. Thus the additional 25% and 35% fluorescence quenching in presence of MP- Ti_4O_7 nanomaterials and Au- doped MP-Ti_4O_7 nanocomposites respectively is solely due to electron transfer from the dye excited state to the conduction band of the nanocomposites.

3.3.2. Time resolved fluorescence emission studies

To shed more light on the electron transfer process discussed above, time resolved fluorescence studies were performed. Earlier studies show that the fluorescent probes when adsorbed on the surface of the quenchers have shorter lifetime values compared to those present in
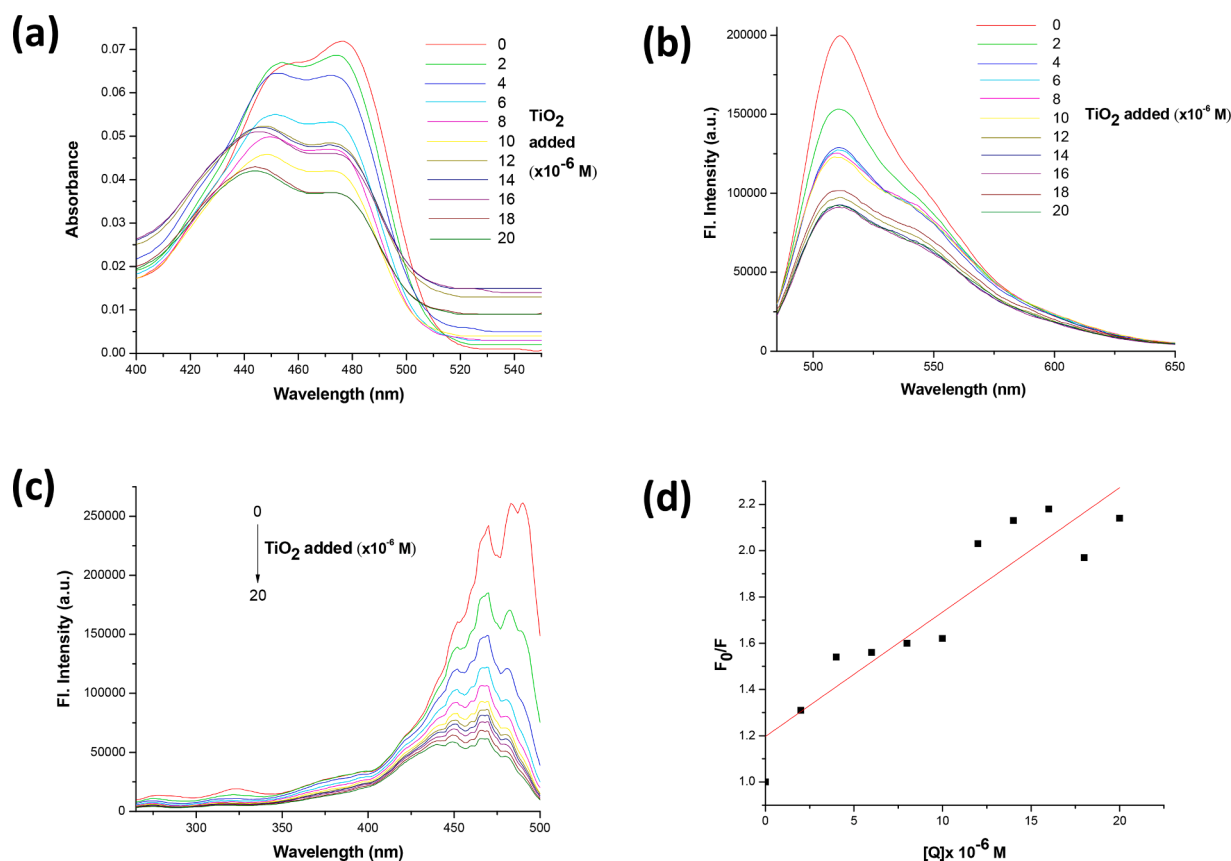

Fig. 8. Fluorescence Quenching of fluorescein dye using MP-Ti_4O_7 nanomaterials; (a) Absorption spectra, (b) Fluorescence emission spectra, λ_{ex} = 475nm, (c) Fluorescence excitation spectra, λ_{em} = 515 nm, (d) Stern- Volmer plot.
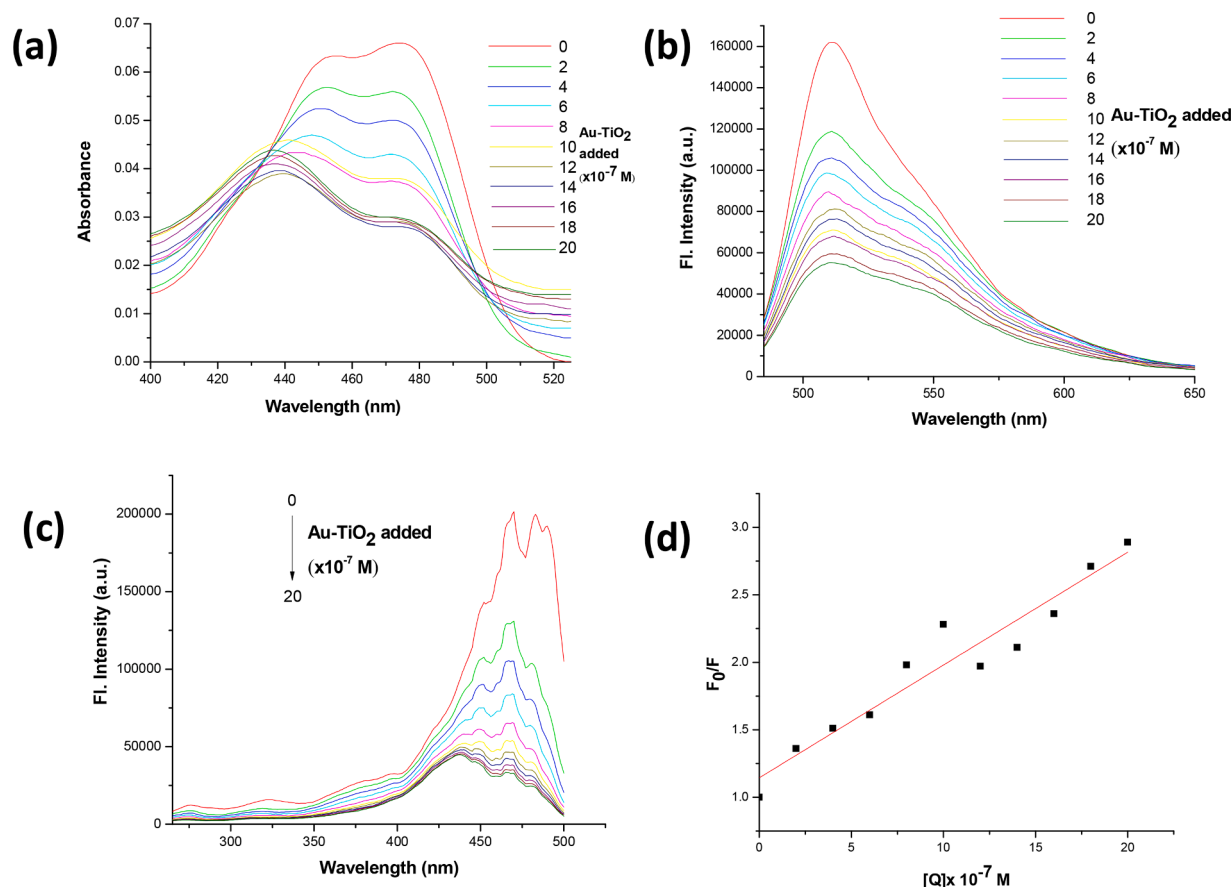
Fig. 9. Fluorescence Quenching of fluorescein dye using Au doped MP-Ti_4O_7 nanocomposites: (a) Absorption spectra, (b) Fluorescence emission spectra, λ_{ex} = 475 nm, (c) Fluorescence excitation spectra, λ_{em} = 515 nm, (d) Stern- Volmer plot.

solution in free the state [65,66]. The time resolved fluorescence results of FL dye in presence of MP-Ti_4O_7 nanomaterials are summarized in Table 2. In the absence of any quencher, the fluorescence lifetime decay was fitted to a single exponential given as [$F(t) = A \exp(-t/\tau)$] and the fluorescence lifetime decay in presence of the nanoparticle / nanocomposites was fitted to a bi-exponential given as [$F(t) = A_1 \exp(-t/\tau_1) + A_2 \exp(-t/\tau_2)$].

The shorter lifetime component (τ_1) arising in presence of MP-Ti_4O_7 nanomaterials is assigned to those dye molecules adsorbed on the surface of the nanomaterials and participating in electron transfer while τ_2 values correspond to free unadsorbed FL molecules in solution. The negative amplitude (a_1) of the shorter τ_1 component indicates growth of a new dye species, i.e., those participating in fast electron transfer with the nanomaterials.

The time resolved fluorescence results of FL dye in presence of Au-doped MP-Ti_4O_7 nanocomposites are summarized in Table 3. In the absence of any quencher, the fluorescence lifetime decay was fitted to a single exponential and the fluorescence lifetime decay in presence of the nanocomposites was fitted to a bi- exponential.

Here too, the growth in the short-lived component can be assigned to

the adsorbed dye molecules which may undergo aggregation on the surface. Thus the emergence of the fast lifetime component τ_1 in the fluorescence decay of FL in presence of both types of nanomaterials confirms fast electron transfer from the dye excited state to the nanomaterials.

The rate of electron transfer (k_{ET}) from the excited state of FL to the conduction band of the nanomaterials can be calculated as [67]

$$k_{ET} = 1/\tau_{ads} - 1/\tau \qquad (3)$$

where τ_{ads} is lifetime of the dye molecules adsorbed on the surface of the nanomaterials and τ is the lifetime of free dye molecules present in the solution. The electron transfer rate is higher in case of Au- doped MP-Ti_4O_7 than in MP- Ti_4O_7 indicating better electron transfer in case of the former nanocomposites.

4. Conclusions

Substoichiometric titanium oxides i.e. Magnéli phase TiO_x are attractive due to the growing demand for conductive materials. However, synthesis of Magnéli phase TiO_x nanoparticles, particularly Ti_4O_7

Table 2
Fluorescence lifetime values of FL in absence and presence of MP-Ti_4O_7 nanomaterials and the rate constant values for electron transfer.

MP-Ti_4O_7 added	τ_1 (ns)	τ_2 (ns)	a_1	a_2	$<\tau>$ (ns)	X^2	$k_{ET} \times 10^9$ (sec^{-1})
0 M		3.508				1.09	——
2×10^{-6} M	1.7352	3.3868	−0.044	1.044	3.4595	1.0317	0.291
6×10^{-6} M	1.6747	3.3284	−0.041	1.041	3.396	1.111	0.297
12×10^{-6} M	1.9878	3.3578	−0.012	1.012	3.374	1.0115	0.218
16×10^{-6} M	1.635	3.2867	−0.035	1.035	3.345	1.116	0.327
20×10^{-6} M	1.63	3.27	−0.036	1.036	3.329	1.053	0.308

Table 3

Fluorescence lifetime values of FL in absence and presence of Au- doped MP-Ti_4O_7 nanocomposites and the rate constant values for electron transfer.

Au-TiO_2 added	τ_1 (ns)	τ_2 (ns)	a_1	a_2	$<\tau>$ (ns)	X^2	$k_{ET} \times 10^9 (sec^{-1})$
0 M		3.508				1.09	——
2×10^{-7} M	1.676	3.336	−0.038	1.038	3.399	1.08	0.312
6×10^{-7} M	1.663	3.297	−0.035	1.035	3.354	1.081	0.316
12×10^{-7} M	1.628	3.262	−0.033	1.033	3.316	1.07	0.329
16×10^{-7} M	1.623	3.24	−0.035	1.035	3.297	1.102	0.331
20×10^{-7} M	1.60	3.23	−0.032	1.032	3.282	1.09	0.34

which has the highest conductivity among all Magnéli phases is challenging. More so because the focus has been on small size and high surface area. One way of increasing the surface area is by reduction of the particle sizes to the nano dimension. In nanomaterials, particles are effectively packed, thus the contact resistance between particles decreases leading to enhanced conductivity.

In this work, MP-Ti_4O_7 nanoparticles and Au doped MP-Ti_4O_7 nanocomposites have been successfully synthesized by citrate mediated sonochemical method using β-CD as a template at ambient temperature. Both the sonochemical method of synthesis as well as use of β-CD leads to the formation of anisotropic nanoparticles of small size 20-30 nm.

One very important area of application of TiO_x nanomaterials is in photocatalysis. The anisotropic MP-Ti_4O_7 nanoparticles and Au doped MP-Ti_4O_7 nanocomposites synthesized in this work function as efficient photocatalysts for the degradation of the dye pollutant Malachite green. Au-doped MP-Ti_4O_7 performs slightly better as photocatalyst due to enhanced electron hole separation in the noble metal doped oxide nanomaterials.

Another equally important application of TiO_x nanomaterials may be in photovoltaic devices. For this, the nanomaterials should be well sensitized by dyes absorbing in the visible part of the spectrum. We have seen that the MP-Ti_4O_7 nanoparticles and Au doped MP-Ti_4O_7 nanocomposites can be effectively sensitized by a xanthene dye, Fluorescein indicating efficient electron transfer from the excited state of the dye to the conduction band of the nanomaterials. This implies that these MP-Ti_4O_7 nanoparticles and Au doped MP-Ti_4O_7 nanocomposites may serve as prospective photoanode materials in dye sensitized solar cells (DSSCs). The electron transfer rate constants from these nanomaterials to FL dye are quite high $\sim 10^8 \ s^{-1}$.

The FEM simulations corresponding to the triangular Au-doped MP-Ti_4O_7 nanocomposites shows large extent of intermediate charge generation in these materials as evident from the interfacial electromagnetic field. The FEM results have shown that interfacial plasmonic charge generation at the metal-semiconductor interface in the Au-doped MP-Ti_4O_7 nanocomposites promotes band electrons across the band gap. This explains the enhanced photocatalytic efficiency of the Au-doped MP-Ti_4O_7 nanocomposites.

Thus the photocatalysis results, FEM results, the fluorescence quenching and the time resolved fluorescence results provide substantive evidence in support of efficient electron transfer from the synthesized nanocomposites to dyes. Thus these materials have the potential of being used as efficient photocatalysts and as photoanode materials in dye sensitized solar cells in the future.

Declaration of Competing Interest

There are no conflicts of interests and no conflict of financial interests to declare.

Data availability

Data will be made available on request.

Supplementary materials

Supplementary material associated with this article can be found, in the online version, at doi:10.1016/j.chphi.2023.100432.

References

[1] V. Adamaki, F. Clemens, P. Ragulis, S.R. Pennock, J. Taylor, C.R. Bowen, Manufacturing and characterization of Magnéli phase conductive fibres, J. Mater. Chem. A. 2 (2014) 8328–8333.

[2] U. Kuylenstierna, A. Magneli, A new modification of titanium monoxide, Acta Chem. Scand. 10 (1956) 1195–1196.

[3] R.F. Bartholomew, D.R. Frankl, Electrical properties of some titanium oxides, Phys. Rev. 187 (1969) 828–833.

[4] S.S. Huang, Y.H. Lin, W. Chuang, P.S. Shao, C.H. Chuang, J.F. Lee, M.L. Lu, Y. T. Weng, N.L. Wu, Synthesis of high-performance titanium sub-oxides for electrochemical applications using combination of sol–gel and vacuum-carbothermic processes, ACS Sustain. Chem. Eng. 6 (3) (2018) 3162–3168.

[5] A.F. Arif, R. Balgis, T. Ogi, F. Iskandar, A. Kinoshita, K. Nakamura, K. Okuyama, Highly conductive nano-sized Magnéli phases titanium oxide (TiO x), Sci. Rep 7 (3646) (2017) 1–9.

[6] J.R. Smith, F.C. Walsh, R.L. Clarke, Electrodes based on Magnéli phase titanium oxides: the properties and applications of Ebonex® materials, J. Appl. Electrochem. 28 (1998) 1021–1033.

[7] R. Zhu, Y. Liu, J. Ye, X. Zhang, Magnéli phase Ti_4O_7 powder from carbothermal reduction method: formation, conductivity and optical properties, J. Mater. Sci.: Mater. Electron. 24 (2013) 4853–4856.

[8] J. Ye, G. Wang, X. Li, Y. Liu, R. Zhu, Temperature effect on electrochemical properties of Ti_4O_7 electrodes prepared by spark plasma sintering, J. Mater. Sci: Mater. Electron. 26 (2015) 4683–4690.

[9] A. Kitada, G. Hasegaw, Y. Kobayashi, K. Kanamori, K. Nakanishi, H. Kageyama, Selective preparation of macroporous monoliths of conductive titanium oxides Ti_nO_{2n-1} (n = 2, 3, 4, 6) J. Am, Chem. Soc. 134 (2012) 10894–10898.

[10] C. Tang, D. Zhou, S. Fang, L. Yang, Effects of Ti_4O_7 on secondary alkaline zinc anode, J. Electrochem. Soc. 159 (2012) A1796–A1800.

[11] P. Krishnan, S.G. Advani, A.K. Prasad, Magneli phase Ti_nO_{2n-1} as corrosion-resistant PEM fuel cell catalyst support, J. Solid State Electrochem. 16 (2012) 2515–2521.

[12] T. Ioroi, H. Senoh, S.I. Yamazaki, Z. Siroma, N. Fujiwara, K. Yasuda, Stability of corrosion-resistant Magneli-phase Ti_4O_7-supported PEMFC catalysts at high potentials, J. Electrochem. Soc. 155 (2008) B321–B326.

[13] D. Portehault, V. Maneeratana, C. Candolfi, N. Oeschler, I. Veremchuk, Y. Grin, C. Sanchez, M. Antonietti, Facile general route toward tunable Magnéli nanostructures and their use as thermoelectric metal oxide/carbon nanocomposites, ACS nano 5 (2011) 9052–9061.

[14] F.C. Walsh, R.G.A. Wills, The continuing development of Magnéli phase titanium sub-oxides and Ebonex® electrodes, Electrochim. Acta. 55 (2010) 6342–6351.
[15] C. Tang, D. Zhou, Q. Zhang, Synthesis and characterization of Magneli phases: Reduction of TiO2 in a decomposed NH3 atmosphere, Mater. Lett. 79 (2012) 42–44.
[16] S. Andersson, B. Collén, U. Kuylenstierna, A. Magnéli, Phase analysis studies on the titanium-oxygen system, Acta Chem. Scand. 11 (1957) 1641–1652.
[17] R. Zhu, Y. Liu, J. Ye, X. Zhang, Magnéli phase Ti4O7 powder from carbothermal reduction method: formation, conductivity and optical properties, J. Mater. Sci.: Mater. Electron. 24 (2013) 4853–4856.
[18] X. Zhang, Y. Lin, X. Zhong, L. Wang, W. Liu, A. Singh, Q. Zhao, Fabrication and characterization of Magneli phase Ti4O7 submicron rods, J. Mater. Sci.: Mater. Electron. 27 (2016) 4861–4865.
[19] G.M. Whitesides, B. Grzybowski, Self-assembly at all scales, Science. 295 (2002) 2418–2421.
[20] Y. Min, M. Akbulut, K. Kristiansen, Y. Golan, J. Israelachvili, The role of interparticle and external forces in nanoparticle assembly, Nat. Mater. 7 (2008) 527–538.
[21] A. Haryono, W.H. Binder, Controlled arrangement of nanoparticle arrays in block-copolymer domains, Small 2 (2006) 600–611.
[22] A.K. Boal, F. Ilhan, J.E. DeRouchey, T. Thurn-Albrecht, T.P. Russell, V.M. Rotello, Self-assembly of nanoparticles into structured spherical and network aggregates, Nature 404 (2000) 746–748.
[23] J. Szejtli, ChemInform abstract: introduction and general overview of cyclodextrin chemistry, Chem. Rev. 98 (1998) 1743–1753.
[24] R. Breslow, S.D. Dong, Biomimetic reactions catalyzed by cyclodextrins and their derivatives, Chem. Rev. 98 (1998) 1997–2011.
[25] S. Polarz, B. Smarsly, L. Bronstein, M. Antonietti, From cyclodextrin assemblies to porous materials by silica templating, Angew. Chem., Int. Ed. 40 (2001) 4417–4421.
[26] M. Chen, G. Diao, E. Zhang, Study of inclusion complex of β-cyclodextrin and nitrobenzene, Chemosphere 63 (2006) 522–529.
[27] R. Aree, N. Chaichit, A new crystal form of β-cyclodextrin/ethanol inclusion complex: channel-type structure without long guest molecules, Carbohydr.Res 338 (2003) 439–446.
[28] G.A. Linde, A. Laverde-Junior, E. Vaz de Faria, N. Barros-Colauto, F. Faria de Moraes, G.M. Zanin, The use of 2D NMR to study β-cyclodextrin complexation and debittering of amino acids and peptides, Food Res. Int. 43 (2010) 187–192.
[29] J. Szejtli, J.L. Atwood, J-M. Lehn, Comprehensive supramolecular chemistry, 3, Pergamon, New York, 1996. Cyclodextrins.
[30] M. Bonini, S. Rossi, G. Karlsson, M. Almgren, P.L. Nostro, P. Baglioni, Self-assembly of β-cyclodextrin in water. Part 1: cryo-TEM and dynamic and static light scattering, Langmuir 22 (2006) 1478–1484.
[31] G. Gonzalez-Gaitano, P. Rodriguez, J.R. Isasi, M. Fuentes, G. Tardajos, M. J. Sanchez, The aggregation of cyclodextrins as studied by photon correlation spectroscopy, J. Incl. Phenom. Macrocycl. Chem. 44 (2002) 101–105.
[32] A. Wu, X. Shen, Y.J. He, Investigation on γ-cyclodextrin nanotube induced by N,N′-diphenylbenzidine molecule, J. Colloid Interface Sci. 297 (2006) 525–533.
[33] T. Huang, F. Meng, F. Qi, Facile synthesis and one-dimensional assembly of cyclodextrin-capped gold nanoparticles and their applications in catalysis and surface-enhanced raman scattering, J. Phys. Chem. C. 113 (2009) 13636–13642.
[34] B. Aswathy, G.S. Avadhani, S. Suji, G. Sony, Synthesis of β-cyclodextrin functionalized gold nanoparticles for the selective detection of Pb2+ ions from aqueous solution, Front. Mater. Sci. 6 (2012) 168–175.
[35] M. Chandrasekar, M. Subash, V. Perumal, S. Panimalar, S. Aravindan, R. Uthrakumar, C. Inmozhi, Abdulgalim B. Isaev, Sudhakar Muniyasamy, A. Raja, K. Kaviyarasu, Specific charge separation of Sn doped MgO nanoparticles for photocatalytic activity under UV light irradiation, Sep. Purif. Technol. 294 (2022), 121189.
[36] V. Perumal, C. Inmozhi, R. Uthrakumar, R. Robert, M. Chandrasekar, S. Beer Mohamed, Shehla Honey, A. Raja, Fahd A. Al-Mekhlafi, K. Kaviyarasu, Enhancing the photocatalytic performance of surface-Treated SnO2 hierarchical nanorods against methylene blue dye under solar irradiation and biological degradation, Environ. Res. 209 (2022) 112821.
[37] S. Panimalar, M. Subash, M. Chandrasekar, R. Uthrakumar, C. Inmozhi, Wedad A. Al-Onazi, Amal M. Al-Mohaimeed, Tse-Wei Chen, J. Kennedy, M. Maaza, K. Kaviyarasu, Reproducibility and long-term stability of Sn doped MnO2 nanostructures: practical photocatalytic systems and wastewater treatment applications, Chemosphere 293 (2022), 133646.
[38] M. Subash, M. Chandrasekar, S. Panimalar, C. Inmozhi, K. Parasuraman, R. Uthrakumar, K. Kaviyarasu, Pseudo-first kinetics model of copper doping on the structural,magnetic, and photocatalytic activity of magnesium oxide nanoparticles for energy application, Biomass Convers. Biorefin. 13 (2023) 3427–3437.
[39] R. Bleta, A. Lannoy, C. Machut, E. Monflier, A. Ponchel, Understanding the role of cyclodextrins in the self-assembly, crystallinity, and porosity of titania nanostructures, Langmuir 30 (2014) 11812–11822.
[40] H. Kochkar, M. Aouine, A. Ghorbel, G. Berhault, Shape-controlled synthesis of silver and palladium nanoparticles using β-cyclodextrin, J. Phys. Chem. C. 115 (2011) 11364–11373.
[41] T.K. Sarma, D. Chowdhury, A. Paul, A. Chattopadhyay, Synthesis of Au nanoparticle–conductive polyaniline composite using H2O2 as oxidising as well as reducing agent, Chem. Commun. 10 (2002) 1048–1049.
[42] A.Y. Baranchikov, V.K. Ivanov, Y.D. Tretyakov, Sonochemical synthesis of inorganic materials, Russian Chem. Rev. 76 (2007) 133–151.
[43] D. Nagao, Y. Shimazaki, S. Saeki, Y. Kobayashi, M. Konno, Effect of ultrasonic irradiation on carbon-supported Pt–Ru nanoparticles prepared at high metal concentration, Colloids Surf. A Physicochem. Eng. Asp. 302 (2007) 623–627.
[44] M.R. Hoffmann, S.T. Martin, W. Choi, D.W. Bahnemann, Environmental applications of semiconductor photocatalysis, Chem. Rev. 95 (1995) 69–96.
[45] A.L. Linsebigler, G. Lu, J.T. Yates, Photocatalysis on TiO2 surfaces: principles, mechanisms, and selected results, Chem. Rev 95 (1995) 735–758.
[46] C. Hachem, F. Bocquillon, O. Zahraa, M. Bouchy, Decolourization of textile industry wastewater by the photocatalytic degradation process, Dyes Pigm 49 (2011) 117–125.
[47] C. Berberidou, I. Poulios, N.P. Xekoukoulotakis, D. Mantzavinos, Sonolytic, photocatalytic and sonophotocatalytic degradation of malachite green in aqueous solutions, Appl. Catal. B: Environ 74 (2007) 63–72.
[48] K.W. Boer, Survey of semiconductor physics volume II: barriers, Junctions, Surfaces, and Devices (1990).
[49] G. Rothenberger, J. Moser, M. Gratzel, N. Serpone, D.K. Sharma, Charge carrier trapping and recombination dynamics in small semiconductor particles, J. Am. Chem. Soc. 107 (1985) 8054–8059.
[50] M. Gratzel, Heterogeneous Photochemical Electron Transfer, CRC Press, Boca Raton, 1989.
[51] M; Toyoda, T; Yano, B; Tryba, S; Mozia, T; Tsumura, M. Inagaki, Preparation of carbon-coated Magneli phases TinO2n−1 and their photocatalytic activity under visible light, Appl. Catal. B: Environ. 88 (2009) 160–164.
[52] S. De, A. Girigoswami, S. Mandal, Enhanced fluorescence of triphenylmethane dyes in aqueous surfactant solutions at supramicellar concentrations—effect of added electrolyte, Spectrochim. Acta - A: Mol. Biomol. Spectrosc. 58 (2002) 2547–2555.
[53] A. Pandikumar, Su-Pei Lim, S. Jayabal, N.M. Huang, H.N. Lim, R. Ramaraj, Titania@gold plasmonic nanoarchitectures: an ideal photoanode for dye-sensitized solar cells, Renew. Sust. Energ. Re. 60 (2016) 408–420.
[54] A. Ayati, A. Ahmadpour, F.F. Bamoharram, B. Tanhaei, M. Manttari, M. Sillanpaa, A review on catalytic applications of Au/TiO2 nanoparticles in the removal of water pollutant, Chemosphere 107 (2014) 163–174.
[55] P.V. Kamat, Quantum dot solar cells. semiconductor nanocrystals as light harvesters, J. Phys. Chem. C. 112 (2008) 18737–18753.
[56] P. Priecel, H.A. Salami, R.H. Padilla, Z. Zhong, J.A. Lopez-Sanchez, Anisotropic gold nanoparticles: preparation and applications in catalysis, Chin. J. Catal. 37 (2016) 1619–1650.
[57] N.D. Burrows, A.M. Vartanian, N.S. Abadeer, E.M. Grzincic, L.M. Jacob, W. Lin, J. Li, J.M. Dennison, J.G. Hinman, C.J. Murphy, Anisotropic nanoparticles and anisotropic surface chemistry, J. Phys. Chem. Lett. 7 (2016) 632–641.
[58] Y. Tian, T. Tatsuma, Mechanisms and applications of plasmon-induced charge separation at TiO2 films loaded with gold nanoparticles, J. Am. Chem. Soc. 127 (2005) 7632–7637.
[59] Z.L. Wang, Characterizing the structure and properties of individual wire-like nanoentities, Adv. Mater. 12 (2000) 1295–1298.
[60] P.B. Johnson, R.W. Christy, Optical constants of the noble metals, Phys. Rev. B. 6 (1972) 4370–4379.
[61] D.E. Aspnes, A.A. Studna, Dielectric functions and optical parameters of Si, Ge, GaP, GaAs, GaSb, InP, InAs, and InSb from 1.5 to 6.0 Ev, Phys. Rev. B. 27 (1983) 985–1009.
[62] S. De, R. Kundu, Spectroscopic studies with fluorescein dye - protonation, aggregation and interaction with nanoparticles, J. Potochem. Photobiol. A. 223 (2011) 71–81.
[63] D. Margulies, G. Melman, A. Shanzer, Fluorescein as a model molecular calculator with reset capability, Nat. Mater 4 (2005) 768–771.
[64] R. Sjoback, J. Nygren, M. Kubista, Absorption and fluorescence properties of fluorescein, Spectrochim. Acta. 51 (1995) L7–L21.
[65] A. Kathiravan, R. Renganathan, An investigation on electron transfer quenching of zinc(II) meso-tetraphenylporphyrin (ZnTPP) by colloidal TiO2, Spectrochim. Acta. Part A. 71 (2008) 1106–1109.
[66] G. Ramakrishna, S. Verma, D.A. Jose, D.K. Kumar, A. Das, D.K. Palit, H.N. Ghosh, Interfacial Electron Transfer between the Photoexcited Porphyrin Molecule and TiO2 Nanoparticles: Effect of Catecholate Binding, J. Phys. Chem. B. 110 (2006) 9012–9021.
[67] S. Biswas, S. De, A. Kathiravan, Ultraslow recombination in AOT-capped TiO2 nanoparticles sensitized by protoporphyrin IX, Dalton Trans 43 (2014) 15065–15074.